Texture, Second-Phase Particles, and the Anisotropy of Deformation Behavior in TTMP AZ61

TRACY D. BERMAN, TRESA M. POLLOCK, and J. WAYNE JONES

The deformation, damage accumulation, and fracture behavior of thixomolded and thermomechanically processed AZ61 were studied by room temperature uniaxial straining. The material was examined in as-molded, as-rolled, and rolled + annealed conditions. The yield strength and work hardening behavior are controlled primarily by grain size and crystallographic texture, which reaches a maximum of only 4.8 multiples of random density in the as-rolled material. The low degree of texture results in a low degree of plastic anisotropy (Lankford r value), suggesting good formability properties. In addition, it is shown that although the β-phase particles begin to crack as early as 4 pct elongation, their presence does not lead to a decrease in ductility, as β-phase cracks do not coalesce to initiate fracture.

DOI: 10.1007/s11661-015-2913-5

I. INTRODUCTION

IT is well known that grain refinement improves both strength and ductility in Mg and its alloys.[1–6] As the grain size is refined strength increases, which can be described by the Hall–Petch relationship. The fracture mechanism also changes with decreasing grain size from intergranular failure to a more ductile rupture by microvoid coalescence in AZ31,[7,8] AZ91,[9] and WE43.[10]

As basal slip is the predominant deformation mechanism, the orientation of the basal planes with respect to the loading direction plays a critical role in the deformation of magnesium alloys. Experiments designed to study the influence of starting texture, independent of grain size, by machining samples at different orientations from a textured plate, show that the orientation of the basal planes relative to the loading direction has a strong effect on both the strength and ductility.[11,12] Reduction of the basal texture in sheet material can lead to dramatic improvements in ductility.[13–16]

The introduction of secondary phases in magnesium alloy sheet has been reported to have both positive and negative effects on ductility. An increase in the volume fraction of the β-phase is associated with a decrease in ductility. Yet, secondary phases can serve to decrease texture by altering the recrystallization mechanisms and kinetics and by stabilizing a fine grain size.[17,18] Since the contribution of β-phase particles to these processes is still not understood in Mg alloys, the property trade off cannot yet be established.

TRACY D. BERMAN, Post-Doctoral Fellow, and J. WAYNE JONES, Professor, are with the Materials Science and Engineering, University of Michigan, 2300 Hayward St, Ann Arbor, MI 48109 Contact-mail: tradiasa@umich.edu. TRESA M. POLLOCK, Professor, is with the Materials Department, University of California, Santa Barbara, CA, 93106-5050

Manuscript submitted November 21, 2014.
Article published online April 22, 2015

Cracking in the β-phase during deformation has been reported in AZ91 by several authors,[9,19–24] as well as in AZ80,[25] AM60,[24] and AM50.[26] In AZ91 alloys with an interconnected network of β-eutectics, cracking in the β-phase can lead to fracture.[21] It has been reasonably hypothesized that even if the β-network is not continuous, the growth and coalescence of the particle-initiated cracks are detrimental to ductility.[20,22,23] Yet in AM60 and AM50, with a lower β-phase volume fraction, there is no evidence that particle cracking results in failure. Whether linkage of cracks in the β-phases plays a role in failure of the material depends on the β-phase volume fraction and morphology, and has yet to be thoroughly investigated.

Decker and co-workers recently developed a new process designated as thixomolded thermomechanical processing (TTMP), which produces Mg alloy sheet by utilizing untextured thixomolded plates as the warm-rolling feedstock.[27,28] Thixomolding is an injection molding process, where the shearing of the liquid metal in the barrel decreases the viscosity, allowing casting at lower temperatures. The rapid solidification rate produces finer grain sizes, an isotropic texture, refined secondary phases, low porosity, and a relatively homogeneous microstructure.[29,30] It has been demonstrated that AZ61 produced by TTMP has a fine grain size, which is assumed to result from grain stabilization by the refined β-$Mg_{17}Al_{12}$ phase.[27] TTMP sheets exhibit very limited edge cracking during rolling, and both the strength and ductility are improved from the as-thixomolded condition. Our studies of TTMP AZ61 sheet have demonstrated a fine grain size and a basal texture intensity less than 5 multiples of random density (MRD), which can be reduced following a recrystallization annealing treatment.[31–35] The aim of the present study is to establish the effects of grain size, texture, and β-$Mg_{17}Al_{12}$ volume fraction on the deformation and fracture behavior of TTMP AZ61 at room temperature.

II. EXPERIMENTAL PROCEDURES

The TTMP process started with 200 mm × 200 mm × 3 mm thixomolded® plates of AZ61. The nominal composition of the alloy, as determined by spectrographic chemical analysis by Dead Sea Magnesium, was Mg-6.5 wt pct Al-0.46 wt pct Zn-0.14 wt pct Mn. Molding parameters were selected by nanoMAG, LLC to result in low porosity and a solid fraction of less than 5 pct. The plates were preheated for 5 minutes at 588 K (315 °C) and then warm-rolled in a single-pass with a roll temperature near 473 K (200 °C). After rolling, the sheets cooled to room temperature in ambient air. The final sheet thickness was 1.8 mm, a thickness reduction of approximately 40 pct.

Dogbone tensile specimens with a gage length of 25.45 mm and a width 6.35 mm (following subsize specimen designation in ASTM E8/E8M-11) were machined from a total of twelve sheets and one unrolled plate. In the sheets, specimens were machined with the tensile axis oriented at 0 deg, 45 deg, and 90 deg from the rolling direction. The specimen thickness was equal to the material thickness, 3 mm for the thixomolded plates and ~1.8 mm for the sheets.

Annealing treatments were conducted after machining to vary the β-phase volume fraction and the α-Mg grain size. A 10 minute annealing treatment at 558 K (285 °C) was selected to provide a fine-grained recrystallized microstructure.[33] Annealing treatments of 573 K (300 °C) for 20 hours and 693 K (420 °C) for 28 hours were selected based on the Mg-Al phase diagram[36] to yield microstructures with a decreased β-phase volume fraction.

Room temperature tensile tests were performed with an Instron 5505B load frame equipped with a 100 kN load cell. A constant displacement rate of 0.01 mm per second resulted in an initial strain rate of 4×10^{-4} s^{-1}. At least four specimens for each condition were loaded monotonically to failure. Another set of at least three specimens was loaded to $\varepsilon = 10$ pct to calculate the Lankford anisotropy factor, or r value.[37] These specimens were also used to study texture evolution during tensile deformation. Yield strength was calculated using the 0.2 pct offset method.

Metallographic specimens were prepared using standard techniques finishing with 1 μm diamond paste. Water was avoided during polishing, instead Buehler MetaDi® fluid was used as lubrication. To reveal grain boundaries, wrought material was etched for 3 seconds at room temperature in a picral solution composed of 10 mL water, 10 mL acetic acid, 4.3 g of picric acid, and 70 mL of ethanol. For the as-thixomolded material, etching for 3 to 5 seconds in a 278 K (5 °C) solution of 60 mL ethanol, 20 mL water, 15 mL glacial acetic acid, and 5 mL of nitric acid produced the best results. The acetic-nitric solution was also used to reveal the β-particle morphology and as the final preparation step for electron backscatter diffraction (EBSD). No etchant was used on samples intended for microprobe analysis or BSE imaging.

For EBSD mapping, a step size of approximately 1/15 of the average grain diameter and a scan area providing for 500 to 1000 grains were used. The general cleaning procedure was (1) neighbor orientation correlation, (2) one iteration of grain dilation, and (3) grain confidence index (CI) standardization. After the cleaning routine, a partition was generated to only retain points with a CI > 0.1. Points not included in the data partition (indicative of regions of β-phase, grain boundaries, or high local deformation) appear black in the EBSD maps.

A second set of scans was used to determine texture. Here, the scan parameters were selected such that the step size would result in an average of 2 to 5 measurements per grain and that the scan area would sample approximately 10,000 grains. At this step size, the definition of grain loses validity, and thus the only "cleaning" process was creation of a partition to drop all of the low (<0.1) CI points. The EBSD pole figures produced in this manner are comparable to those produced using XRD.[38] Texture was measured near mid-thickness, though comparison to the texture obtained at the surface shows negligible differences. Texture analysis was performed using MTEX, a MATLAB® toolbox.[39]

III. RESULTS AND DISCUSSION

A. *Microstructure*

Figure 1 summarizes the variations in α-Mg grain size, β-particle volume fraction, and texture as a function of processing.

The microstructure of the thixomolded plate is composed of fine α-Mg grains (darker gray) surrounded by blocky β-particles and some divorced β-eutectic (brighter gray) (Figure 1(a)). Some of the brighter particles are Al-Mn intermetallics. Due to rapid solidification, the β-phase volume fraction is 4 pct, lower than the 10 pct expected at equilibrium. The average grain diameter of the as-thixomolded material is 4.3 μm. The cast plate is essentially untextured, which was desirable to aid in producing rolled sheet with low texture.

Rolling results in a highly deformed microstructure. Though there are small regions which undergo dynamic recrystallization,[33,38] the majority of α-Mg grains contain a high internal misorientation. This misorientation results in poor quality EBSD patterns; as a result, a large portion of the as-rolled inverse pole figure (IPF) map is populated by black, non-indexed pixels (Figure 1(b)).

Due to the increased time at temperature during the pre-heat and rolling stages, the volume fraction of β-particles increases to 8 pct. The β-particles deform with the matrix. The particles, as well as the network of particles surrounding the as-molded α-Mg grains, become elongated in the rolling direction (RD).[38]

The as-rolled sheet has a split, near-basal texture with a maximum intensity of 4.8 multiples of random density (MRD). The basal texture exhibits a broad spread along the transverse direction (TD), indicating that the c-axis of some of the grains is tilted away from the normal direction (ND) and toward the TD.

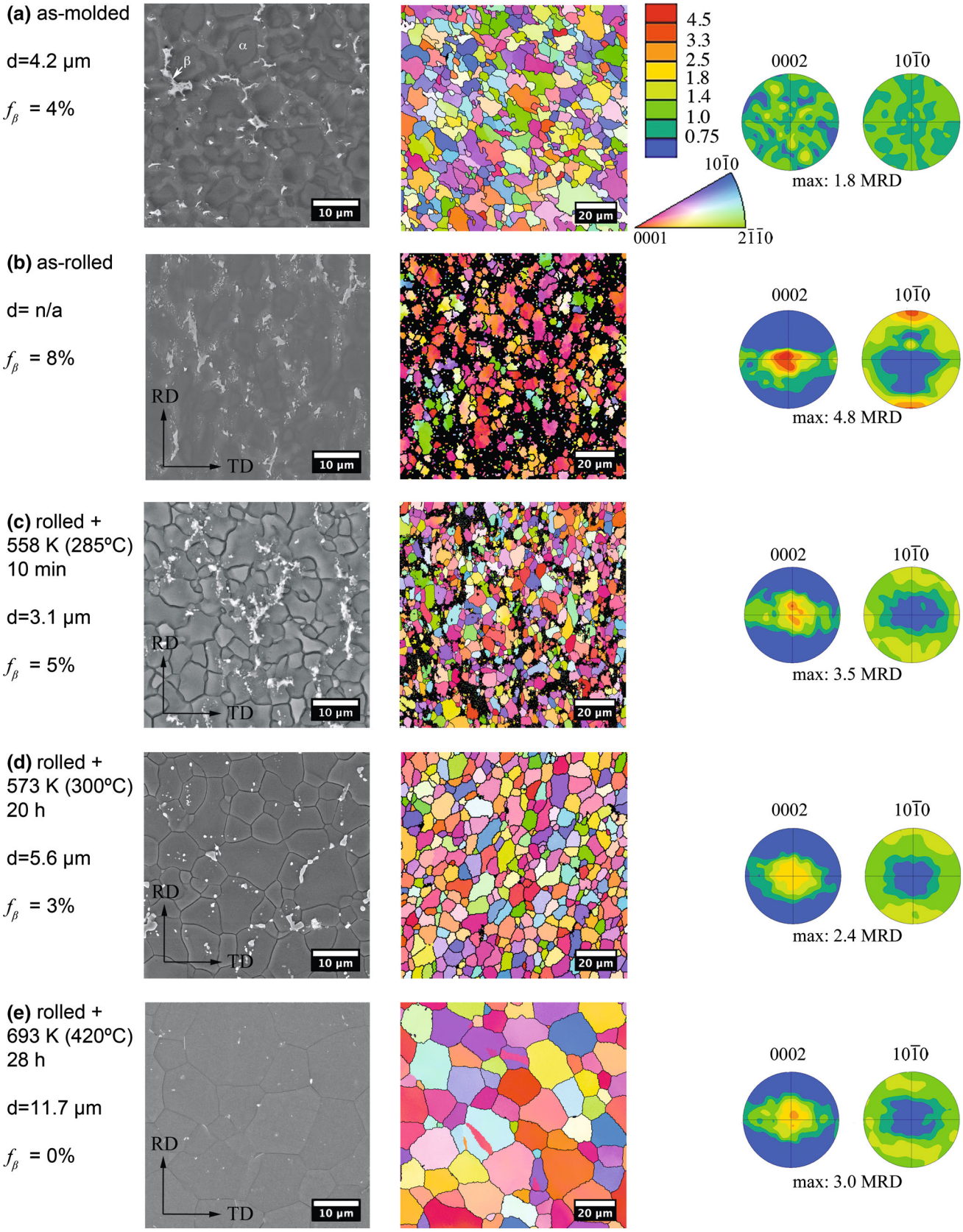

Fig. 1—SE micrographs, EBSD IPF maps, and pole figures summarizing the microstructure and texture of the (*a*) as-molded plate, (*b*) as-rolled sheet, and rolled sheets annealed at (*c*) 558 K (285 °C) for 10 min, (*d*) 573 K (300 °C) for 20 h, and (*e*) 693 K (420 °C) for 28 h. (For interpretation of the figure legend, the reader is referred to the web version of this article.).

The three post-rolling annealing treatments, 558 K (285 °C) for 10 minutes, 573 K (300 °C) for 20 hours, and 693 K (420 °C) for 28 hours, result in a recrystallized microstructure (Figures 1(c) through (e)). The average grain sizes following annealing are 3.1, 5.6, and 11.7 μm, respectively. The volume fraction of the β-phase decreases as the temperature nears, and then exceeds the β-solvus. The β-phase volume fraction is reduced to zero following 693 K (420 °C) for 28 hours; the bright phases visible in Figure 1(e) are Al-Mn intermetallics as determined by energy dispersive spectroscopy. The maximum texture intensity of the basal pole figure decreases to between 2.4 and 3.5 MRD following the annealing treatments.

The difference in grain size and β-phase volume fraction resulting from TTMP and annealing allows us to study the effect of these parameters on the mechanical properties. Unfortunately, as the β-particles provide for grain size stability *via* Zener pinning,[38] grain size and volume fraction could not be varied independently in the present study. In addition, the basal texture intensity after each of these thermal treatments is slightly different as well.

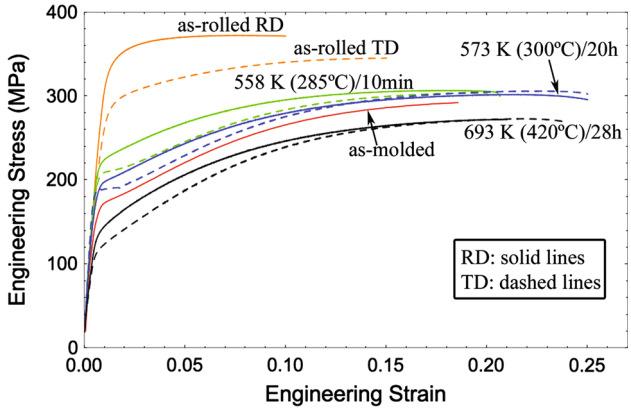

Fig. 2—Tensile deformation behavior of thixomolded plates and TTMP AZ61 sheets when loaded parallel to either the RD or TD. Representative curves are terminated at the average strain at failure.

B. *Tensile Behavior*

Representative monotonic tensile curves of the as-thixomolded plate, as-rolled sheet, and annealed sheets loaded along the RD and TD are shown in Figure 2. Table I summarizes the tensile properties for these conditions as well as the results of tests in which the loading direction was 45 deg from the RD. There was very little scatter in the yield or tensile strength of any of the materials, with a maximum sample-to-sample scatter of 14 MPa. There was much more variability in ductility. The difference in elongation to failure between the most ductile and least ductile specimens was as little a 1 pct strain for some conditions and as large as 13 pct strain for other conditions. It was also observed that the average ductility between sheets could vary by 2 pct.

The as-molded plate exhibited a yield strength of 160 MPa and an average ductility of 19 pct. Rolling results in a twofold increase in yield strength. The deformation following rolling leads to a reduction in the ductility.

In the sheet annealed for 558 K (285 °C) for 10 minutes, the establishment of a recrystallized grain size of about 3 μm resulted in a decrease in the yield strength to 220 MPa. The yield strength was further reduced following both the 573 K (300 °C) for 20 hours and 693 K (420 °C) for 28 hours annealing treatments. The average elongation to failure following annealing was 20 to 26 pct. An average elongation to failure of 23 pct gives the sheet annealed for 10 minutes at 558 K (285 °C), a good balance of strength and ductility.

For all sheet conditions, the orientation dependence of the tensile properties can be summarized: (1) the yield stress is highest along the RD for all conditions and decreases with increasing angle from the RD and (2) work hardening is highest along the TD for all conditions and decreases as the orientation approaches the RD. This anisotropy is the greatest in the as-rolled sheet and decreases following annealing. In the as-rolled sheet, the elongation to failure along the TD is 15, 50 pct higher than along the RD. For the annealed sheets, the elongation to failure and ultimate tensile strength (UTS) are insensitive to orientation.

The contribution of grain size to the yield strength of the material is given by the Hall–Petch relationship

Table I. Tensile Properties of As-Molded Plate and TTMP AZ61 Sheet

Condition	Orientation	YS (MPa)	UTS (MPa)	El. (Pct)
As-molded	—	160	320	19
As-rolled	0 deg	320	370	10
As-rolled	45 deg	270	345	17
As-rolled	90 deg	260	345	15
558 K (285 °C)/10 min	0 deg	220	310	22
558 K (285 °C)/10 min	45 deg	215	310	26
558 K (285 °C)/10 min	90 deg	210	310	20
573 K (300 °C)/20 h	0 deg	190	300	22
573 K (300 °C)/20 h	45 deg	185	300	25
573 K (300 °C)/20 h	90 deg	185	305	25
693 K (420 °C)/28 h	0 deg	140	270	21
693 K (420 °C)/28 h	90 deg	120	270	24

Properties are given as an average, based on testing 3 to 8 samples.

$$\sigma_{gs} = \sigma_o + kd^{-1/2}, \quad [1]$$

where σ_o is the lattice resistance to slip, k is the Hall–Petch coefficient, and d is the average grain size in the material. Using the 0.2 pct offset yield strength (Table II) and the grain sizes given in Figure 1, the Hall–Petch slope for the annealed sheets is found by fitting a linear slope to σ_{YS} *vs* $d^{-1/2}$. The Hall–Petch coefficient can be orientation dependent in textured hcp materials;[40–43] however, due to the limited data available, the yield strength for all sheet orientations was used for fitting. As strain hardening is an important mechanism in the as-rolled sheet, it was not included in this analysis. The best-fit parameters for σ_o and k are 51 MPa and 9.4 MPa × $mm^{1/2}$, respectively. This value of k is comparable to those reported in studies of Mg-Al and Mg-Zn sheets.[44,45]

Figure 3 plots yield stress against $d^{-1/2}$ for thixomolded and TTMP AZ61 as well AZ31,[5,8,46–51] AZ61,[46,52] AM60,[53,54] and AZ91.[46,54,55] Though such a plot is useful for establishing grain size strengthening behavior, texture complicates the relationship. The Hall–Petch constants are decided by the critical resolved shear stress of the active slip systems and by the Taylor factor, both which are texture dependent.[56–58] As a result of the strong basal texture of conventionally wrought materials, many grains are oriented unfavorably for basal slip and prismatic slip must accommodate a higher percentage of tensile deformation than it would in cast materials. Due to the higher critical resolved shear stress of prismatic slip, increasing basal texture intensity leads to an apparent increase of σ_o. In Figure 3, the gray and blue bands distinguish between materials processed by methods associated with strong basal texture (conventional extrusion and rolling) and no texture, or a weaker basal texture [casting, multiple pass equal channel angular pressing (ECAP), and differential speed rolling (DSR)]. Texture can play a more significant role in yield stress than solid solution or precipitation strengthening.

Table II. Fraction of Grains Favorably Oriented for Basal Slip Per Condition

Condition	Orientation	Favorable (Pct)
As-molded	—	24
As-rolled	0 deg	13
As-rolled	45 deg	18
As-rolled	90 deg	20
558 K (285 °C)/10 min	0 deg	17
558 K (285 °C)/10 min	45 deg	21
558 K (285 °C)/10 min	90 deg	20
573 K (300 °C)/20 h	0 deg	18
573 K (300 °C)/20 h	45 deg	20
573 K (300 °C)/20 h	90 deg	22
693 K (420 °C)/28 h	0 deg	18
693 K (420 °C)/28 h	90 deg	22

The yield stress of the as-thixomolded plates falls nearly 40 MPa below that predicted by the TTMP AZ61 Hall–Petch relationship due to the lack of texture in the plates. Alternatively, the as-thixomolded yield stress is in good agreement with a Hall–Petch relationship derived from the literature on cast AM60,[53,54] with σ_o and k equal to 36 and 8.1 MPa × $mm^{1/2}$. While some fine β-precipitates were observed in the TTMP AZ61 sheets by TEM,[33] based on the precipitate size and heterogeneous distribution and the availability of Al in the TTMP AZ61, Orowan strengthening does not contribute to the difference in strength between the cast and wrought material.[38]

The relative activity of prismatic and basal slip is dictated by the variations in the texture intensity and texture components, which affect the fraction of grains oriented for "easy" basal slip.[58] Basal slip is most favorable when the basal plane fiber is tilted 45 deg from the tensile axis. We can determine the fraction of EBSD data points (roughly proportional to the fraction of grains) oriented for soft basal slip by calculating the fraction of EBSD orientations within a certain radius of this fiber; here we use 10 deg. A radius of 10 deg contains 25 pct of the orientations in an isotropic material $((2 * \int_0^{2\pi} \int_{35^\circ}^{55^\circ} r^2 \sin \pi d\theta d\phi)/4\pi r^2)$. Grains with an orientation such that their c-axis falls within the ring in Figure 4(a) are considered favorably oriented for

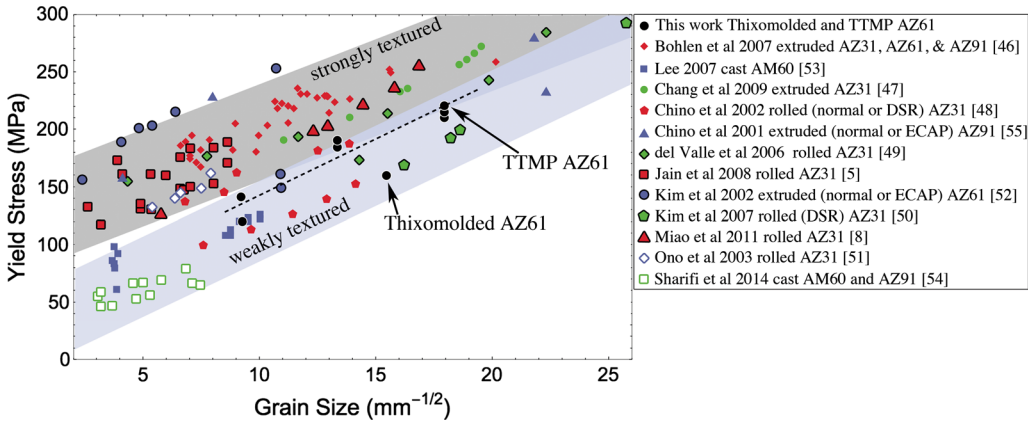

Fig. 3—Hall–Petch plots for the yield stress in thixomolded and TTMP AZ61 compared with tensile yield stress data on AM and AZ series alloys from the literature.[5,8,46–55]

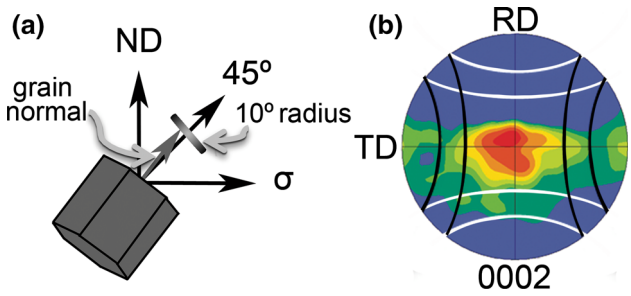

Fig. 4—(*a*) Schematic illustration of the criteria used to identify grains favorably oriented for basal slip when loaded along σ. (*b*) The white and black bands identify the orientations of grains favorable for basal slip when loaded along the RD and TD, respectively.

basal slip. EBSD point orientations falling within the white bands imposed on the basal pole figure of the as-rolled material in Figure 4(b) illustrate the area favorably oriented for basal slip along the RD, while those within the black bands are oriented for easy basal slip along the TD. The results of this calculation for the three orientations studied are summarized in Table II.

For each sheet condition, fewer grains are oriented favorably for basal slip along the RD than along the TD, and therefore, more of the deformation must be accommodated by mechanisms with a higher CRSS than basal slip. Therefore, we observe that σ_{YS} is higher along the RD due to a higher value of σ_o in that direction. This is consistent with viscoplastic self-consistent (VPSC) modeling which has demonstrated that with a tilted basal texture, the loading direction in which prismatic slip accommodates a higher fraction of the strain has a larger yield stress.[58] The ratio of the percent of favorable grains along the RD to the percent of favorable grains along the TD correlates with the difference in σ_{YS}. The as-rolled sheet exhibits the lowest ratio at 0.65, and the largest anisotropy. The annealed sheets have ratios above 0.8, and no more than 20 MPa difference in σ_{YS} between the RD and TD.

Rare-earth-containing alloys, which, similar to TTMP AZ61, exhibit a broad spread along the TD of the basal pole figure, have a higher yield strength when loaded parallel to the RD compared to the TD.[59] Materials with the conventional texture, such as AZ31 sheet, exhibit a higher yield strength along the TD than along the RD, which is directly related to the broader spread of the *c*-axis along the RD than along the TD.[58,60] Through VPSC simulations, Agnew[58] observed that up to 80 pct of the strain in AZ31 loaded in the TD orientation was accommodated by non-basal slip.

C. *Work Hardening Behavior*

Similar to the yield strength, the work hardening response is also dependent on both the grain size and texture. Hollomon's equation

$$\sigma_T = K\varepsilon_T^n, \qquad [2]$$

models work hardening as a power law relationship (with strain hardening exponent, n) between the true stress (σ_T) and the true strain (ε_T). The strain hardening exponent, n, was determined by fitting Eq. [2] to the experimental data (converted to a true stress–strain curve) between 5 and 15 pct ε_T. If the log–log plot of the true stress–strain curve became non-linear, or the strain at failure was reached before 15 pct ε_T, the upper limit on ε_T was decreased.

Table III. Strain Hardening Exponent of As-Molded Plate and TTMP AZ61 Sheet

Condition	Grain Size (μm)	n_0	n_{45}	n_{90}
As-molded	4.3	0.34	—	—
As-rolled		0.07	0.11	0.15
558 K (285 °C)/10 min	3.1	0.21	0.24	0.28
573 K (300 °C)/20 h	5.6	0.27	0.30	0.35
693 K (420 °C)/28 h	11.7	0.32		0.39

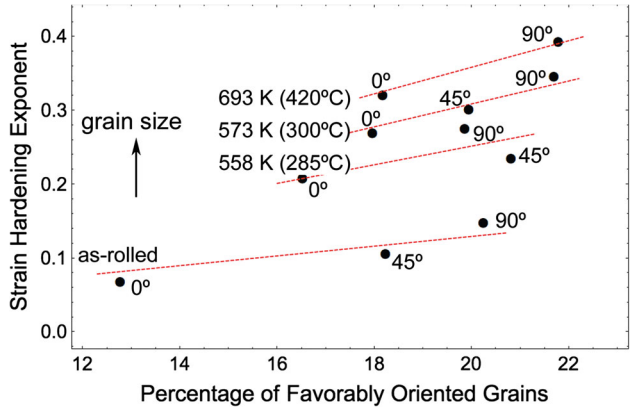

Fig. 5—The effect of grain size and texture (as expressed as the percentage of grains favorably oriented for basal slip) on the strain hardening exponent.

Table III summarizes the average strain hardening exponent calculated for each of the as-molded plate and TTMP sheet conditions. Figure 5 plots n as a function of the percentage of grains oriented favorably for basal slip. In the sheets, the strain hardening exponent increases with increasing grain size, and increases with increasing favorability of basal slip.

A relationship between grain size and work hardening is consistent with the rate of dislocation storage decreasing with decreasing grain size.[49] Higher strain hardening exponents indicate more resistance to shear localization, and thus should predict materials with better formability.[61]

D. *Texture Evolution During Deformation*

The texture evolution after 10 pct deformation in tension also indicates that prismatic slip is decreased and basal slip activity is increased in the more weakly textured materials. During tensile deformation, slip leads to a rotation of the lattice such that the active slip direction tends to become aligned along the tensile axis and the active slip plane parallel to the tensile stress axis. Therefore, texture evolution during deformation provides an insight about the relative slip system

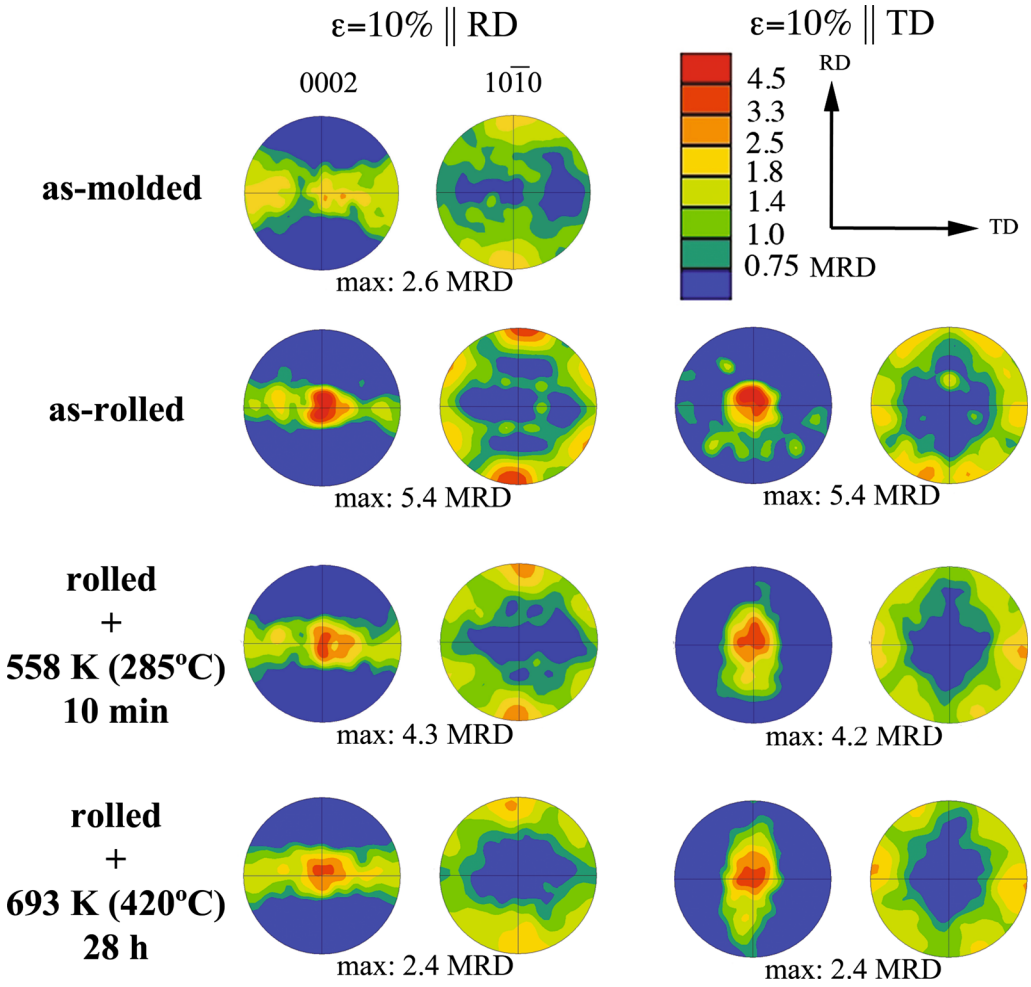

Fig. 6—Texture evolution after 10 pct deformation in tension along the RD (left) and TD (right). The initial textures are provided in Fig. 1. (For interpretation of the figure legend, the reader is referred to the web version of this article.).

activity. Figure 6 summarizes the texture evolution of samples loaded to $\varepsilon = 10$ pct along either the RD or TD.

After deformation, the originally untextured as-molded plate manifests a tight distribution along the TD in the basal pole figure and two strong peaks parallel to the tensile axis in the prismatic pole figure. Sheets loaded along the RD exhibit similar characteristics, with two notable differences, (1) the distribution along the TD is tighter and (2) evidence of sixfold symmetry arises in the prismatic pole figure. In sheet loaded along the TD, the spread along the tensile axis in the basal pole figure is reduced, and the intensity perpendicular to the tensile axis increases. In addition, sixfold symmetry develops in the prismatic pole figures; the two strongest peaks in the prismatic pole figure are along the tensile axis in the annealed sheets. The six peaks appear to be roughly equal in the as-rolled sheet.

The spread in the basal pole figure perpendicular to the tensile axis and the strong peaks in the prismatic pole figure parallel to the tensile axis are a result of basal slip. Basal $\langle \mathbf{a} \rangle$ slip tends to rotate the c-axis such that it becomes perpendicular to the tensile axis. This concentrates the intensity perpendicular to the tensile axis, resulting in an increase in the maximum basal texture intensity.[62–64] For samples loaded along the TD, the original spread of grains along the TD is reduced as the basal plane of these favorably oriented grains rotates toward the RD.

The sixfold symmetry in the prismatic pole figures is a consequence of $\langle \mathbf{a} \rangle$ slip on prismatic planes.[5,60,64,65] Double slip on the prismatic planes leads to the alignment of the $[10\bar{1}0]$ direction with the tensile axis.[64]

Comparing the materials with the weakest and strongest initial textures, the as-molded plate and the as-rolled sheet, provides a qualitative understanding of the relative slip activity. The sixfold texture component does not develop in the as-molded material. Basal slip was dominant in this untextured material. The as-rolled sheet has the smallest fraction of grains favorably oriented for basal slip when loaded along the RD, and therefore, non-basal slip must accommodate a larger fraction of the deformation. Correspondingly, the texture of the as-rolled sheet loaded along the RD displays the strongest sixfold component, indicating increased prismatic slip activity.

A more quantitative description of the relative activity of different slip systems can be obtained by modeling that explicitly considers individual slip systems and their role in evolving texture. Agnew *et al.*[60] used a vis-

coplastic self-consistent (VPSC) model to study tensile deformation in a commercial AZ31 sheet. Though this sheet started with a stronger basal texture (>9 MRD) and less spread along the TD, the texture evolution at ε~11 pct is quite similar to that observed here in the TTMP AZ61 sheets at 10 pct strain. The aggregate response of the crystal rotations will also determine the width and thickness strains that develop during deformation, so the *r* value can be modeled *via* VPSC. Agnew *et al.* found the experimental *r* value and texture evolution were best replicated by assuming that the critical resolved shear stress at room temperature for prismatic slip was 2.5 times that for basal slip; experimentally measured *r* values are considered in more detail in the following section.

As a final note on the texture evolution, there is an additional texture component that may arise during deformation of conventionally processed Mg sheets that was not observed here in the TTMP AZ61 sheets. This component involves $\{10\bar{1}2\}$ extension twinning during tensile deformation and results in the rotation of the *c*-axis of grains from the normal direction of the sheet 86 deg toward the sheet direction perpendicular to the tensile axis.[5,66] Metallography and EBSD at ε = 10 pct indicate that extension twins account for 6 pct of the area in the largest-grained material, the sheet annealed for 693 K (420 °C) for 28 hours. In the finer grained materials, twinning accounted for less than 1 pct of the total area. Twinning is reported more frequently in materials with a grain size larger than 10 μm, and is suppressed by grain refinement.[67,68] As a result of the unique processing path with initially fine-grained thixomolded material, twinning plays a minor role in tensile deformation of the present TTMP AZ61.

Table IV. *r* Values in As-Rolled and Annealed Sheet

	As-Rolled	558 K (285 °C) 10 min
r_0	1.48	0.96
r_{45}	1.59	1.14
r_{90}	1.10	1.09
$\bar{r}$	1.44	1.12
Δr	0.30	0.12
Δr_2	0.49	0.18

Measured at 10 pct tensile deformation.

E. *Lankford r Value*

In order to evaluate the potential formability of the experimental materials studied here, selected tensile tests of the as-rolled sheet and 558 K (285 °C)/10 minutes sheet were interrupted at 10 pct strain for measurement of the width and thickness strains ($\varepsilon_w = \ln(w_f/w_i)$ and $\varepsilon_t = \ln(t_f/t_i)$, where w_f and w_i are the final and initial widths and t_f and t_i are the final and initial thicknesses). Based on these measurements, the Lankford *r* value for each orientation can be determined:

$$r = \frac{\epsilon_w}{\varepsilon_t} \quad [3]$$

The *r* value of the three orientations is used to calculate $\bar{r}$:

$$\bar{r} = \frac{|r_0 + 2 * r_{45} + r_{90}|}{4}. \quad [4]$$

The results are summarized in Table IV. The *r* value and $\bar{r}$ provide indicators of the degree of material formability. In general, a high $\bar{r}$ value indicates that the material resists thinning and should have good drawing properties.[37,69,70] In low-carbon steel and aluminum alloys, a high level of $\bar{r}$ indicates favorable drawability of the material.[71] However, in hcp materials, a high $\bar{r}$ value is associated with strong anisotropy and poor formability, and thus requires a different interpretation.[62] Instead, reduced $\bar{r}$ values in Mg sheet indicate good formability for stretching operations.[59,62,72] The $\bar{r}$ values for the TTMP AZ61L sheet material are all quite low for a Mg sheet alloy, even in the as-rolled condition. Average *r* values of 3 or more are typical in commercial AZ31 sheets.[60]

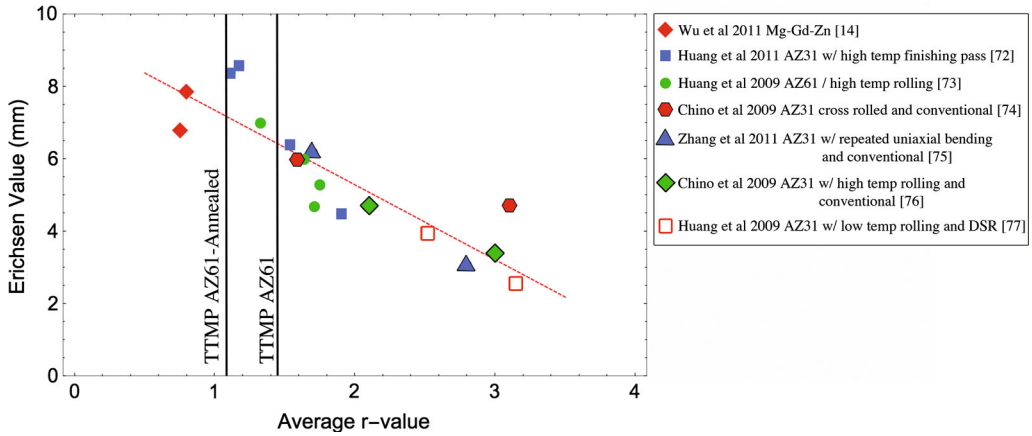

Fig. 7—Relationship between the maximum dome height achieved in Erichsen biaxial stretch tests and the average *r* value of the Mg alloy sheet. Data obtained from the literature.[14,71–76] The vertical lines represent the average *r* value in the as-rolled and annealed [558 K (285 °C) for 10 min] TTMP AZ61 sheets.

For comparison to the present results, Figure 7 is a compilation of results from the literature[14,72–77] illustrating the association between the $\bar{r}$ value and room temperature formability. The maximum dome height, achieved in a standard Erichsen biaxial stretch test, decreases as $\bar{r}$ increases. Assuming a linear relationship between $\bar{r}$ and the Erichsen dome height, as indicated in Figure 7, the literature suggests that based on $\bar{r}$ in the as-rolled and annealed [558 K (285 °C)/10 minutes] TTMP AZ61 sheet, dome heights of 6 to 7 mm might be expected.

Calculation of Δr provides an indication of anisotropy, and predicts the extent of earing.[78]

$$\Delta r = \frac{|r_0 - 2\times r_{45} + r_{90}|}{2}. \quad [5]$$

Bohlen *et al.*[59] suggest that earing in the hcp Mg crystal structure might be better predicted by instead considering the maximum variation of the r value in the sheet, $\Delta r_2 = r_{max} - r_{min}$. In the TTMP AZ61 sheet annealed for 10 minutes at 558 K (285 °C), Δr_2 is 0.18, which is very low. To the authors knowledge, the only lower value that has been reported (or calculated from reported values) is 0.10 in hot rolled ZE10.[59] Values of 1 or more for Δr_2 are not uncommon in Mg sheet.[46,48,60,62,74–77,79–81] In TTMP AZ61, Δr is also quite low, comparable with values in RE alloys.[59] Values of at least 0.3 are typical for Δr.[14,48,59,60,62,74,76,79–81]

As discussed earlier, the r value is strongly dependent on texture.[82] Looking again at the same studies referenced in Figure 7, it is clear that $\bar{r}$ is strongly related to the maximum basal texture intensity. Values from the as-rolled and annealed TTMP AZ61 sheet are consistent with the correlation. The low r value parameters of TTMP AZ61 sheets are a direct consequence of the relatively weak texture of the material. Though room temperature formability was not studied in this work, the favorable $\bar{r}$ and Δr_2 measurements, as well as the high work hardening exponent, indicate that TTMP AZ61 sheets should perform better than commercial AZ31 sheets during ambient forming operations.

F. *Damage Accumulation and Failure*

It is a common thought that cracking in the β-phase initiates tensile fracture in Mg-Al alloys. In order to assess the contribution of the β-phase to failure, damage accumulation during deformation was studied using interrupted tensile tests. In order to understand the mechanisms of damage initiation, specimens were loaded to a specific plastic strain and then unloaded, polished, and examined in the SEM. The tensile curves for an interrupted test along the RD of sheet annealed for 10 minutes at 558 K (285 °C) are given in Figure 8. After a tensile specimen was reloaded, there was a small increase in yield strength; otherwise, the properties of the interrupted tests were equivalent to those found in the monotonic tests. The initial samples were examined after 1, 2, 4, 8, and 16 pct plastic strain. No damage was observed at 1 or 2 pct, so these steps were dropped in further work.

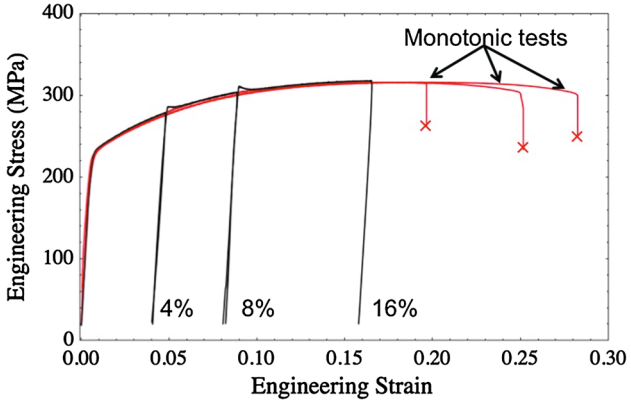

Fig. 8—Interrupted and monotonic stress–strain curves along the RD of sheet annealed for 558 K (285 °C) for 10 min.

The first signs of damage in the microstructure are observed at 4 pct plastic strain. At this point, cracks begin to appear in the β-particles. The number density of cracks increases with increasing strain. Figure 9 shows some of these cracks at (a) ε = 25 pct (failure). The majority of the voids are associated with cracks through the β-phase, and not debonding of the particles with the matrix. The voids are confined almost exclusively to the β-network, even near the fracture surface. No propagation of cracks into the matrix is observed. The extent of cracking corresponds to the β-particle size and volume fraction. Crack length corresponds to the particle dimensions, and the number density of cracks scales with the β-phase volume fraction. In the solution-treated sheet, [693 K (420 °C)/28 hours] damage is not observed until failure, and is only evident very near the fracture surface.

Despite cracking in the particle-containing materials as early as ε = 4 pct, ductility is no lower than that observed in the solution-treated sheet. Therefore, damage associated with the β-phase in TTMP AZ61 sheets has an insignificant impact on ductility. Examination of tensile specimens polished to mid-width post-mortem shows minimal evidence of coalescence of the voids associated with the β-phase (Figure 10).

Macroscopically, shear fracture terminated tensile deformation. The average shear angle relative to the tensile axis is 50 deg in the as-rolled and annealed sheets and 60 deg in the as-molded plates. The average is slightly higher in the as-molded condition as a few of the specimens had shear angles of ~70 deg. The higher shear angles, and lower ductility in some of the as-molded specimens may be a result of the porosity in this condition. In Mg alloys, failure commonly occurs near the plane of maximum shear stress.[83] Attempts to observe the formation of shear bands on tensile specimens polished before deformation were unsuccessful, so it is likely that failure occurs soon after shear localization. Similarly, necking was limited and observed in only a few of the higher ductility samples.

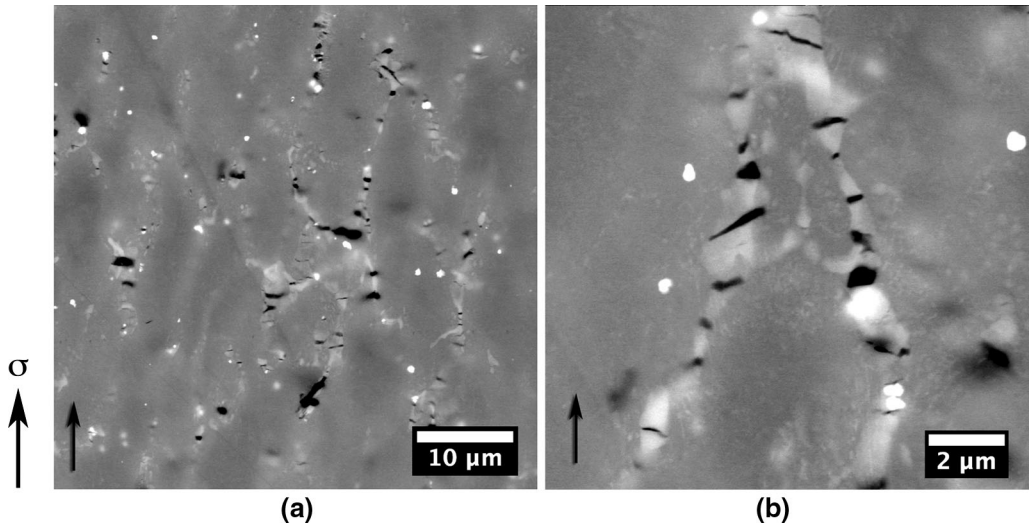

Fig. 9—Damage in the β-phase network after 25 pct tensile deformation along the RD in TTMP AZ61 sheet annealed for 558 K (285 °C) for 10 min.

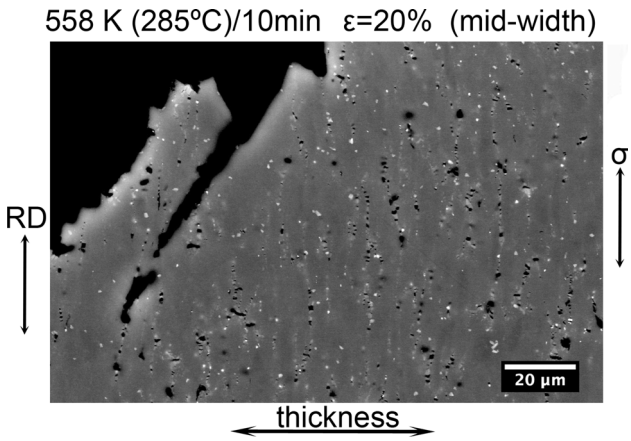

Fig. 10—Damage near the fracture surface in sheet annealed for 558 K (285 °C) for 10 min and loaded along the RD. The majority of the voids are associated with β-particles.

Fractography indicates that microvoid coalescence is the dominant failure mechanism for all of the material conditions. Figure 11 compares the fracture surfaces of the (a) as-molded and (b) as-rolled materials as well as sheets annealed for either (c) 558 K (285 °C) for 10 minutes or (d) 693 K (420 °C) for 28 hours. The dimples are finest in the as-rolled sheet, and in the other materials, the dimple size is on the order of a few micrometers. In the largest-grained material, sheet annealed for 693 K (420 °C) for 28 hours, several coarser features were also observed. These features indicate a transition to a more cleavage-type failure due to the larger grain size. A few of the cleavage-like features with dimensions of 50 to 100 μm were observed in an as-molded sample, as well. Based on their size, these are likely associated with the fracture of grains that solidified prior to injection.

Fragmented β-particles, such as those highlighted by arrows in Figure 12, are observable in many of the pores. Based on observations of failed specimens at mid-width, such as the one shown in Figure 10, this can be attributed to the intersection of the microvoids nucleating in the shear band with voids associated with the β-phase. The particles themselves are not directly responsible for failure, though they may affect the path of the shear localization.

Microvoid coalescence has been observed by several authors in Mg alloy sheets.[7,19,84–87] Grain size is one of the most important parameters in controlling the failure mode of Mg alloy sheets, a brittle to ductile transition can be observed with grain refinement.[8–10] Based on the literature, 10 μm seems to be a benchmark below which microvoid coalescence is the dominant mechanism, though some larger-grained materials, such as 41 μm SiC reinforced AZ91 studied by Luo,[19] also exhibit uniform dimples. Fractography in the TTMP AZ61 is consistent with an evolution in the failure mode to include more cleavage-like behavior as the grain size exceeds 10 μm.

The average ductility to failure in TTMP AZ61 was nominally 23 pct in the annealed sheets, regardless of grain size, β-phase volume fraction, or loading direction. Indeed, referring back to the seminal work by Chapman *et al.*,[1] demonstrating the benefits of grain refinement on ductility, the average room temperature ductility of extruded, commercially pure Mg with comparable grain sizes was between 20 and 28 pct. The presence of the β-phase in TTMP AZ61 does not lead to a decrease in ductility. Additional work is needed to understand how cracking of the β-phase during forming will effect the corrosion and fatigue properties in order to optimize the alloy and processing.

IV. CONCLUSIONS

The tensile properties of TTMP AZ61 are controlled primarily by grain size and crystallographic texture. In the annealed sheets, yield strength varied in accordance with the Hall–Petch relationship, though texture affect-

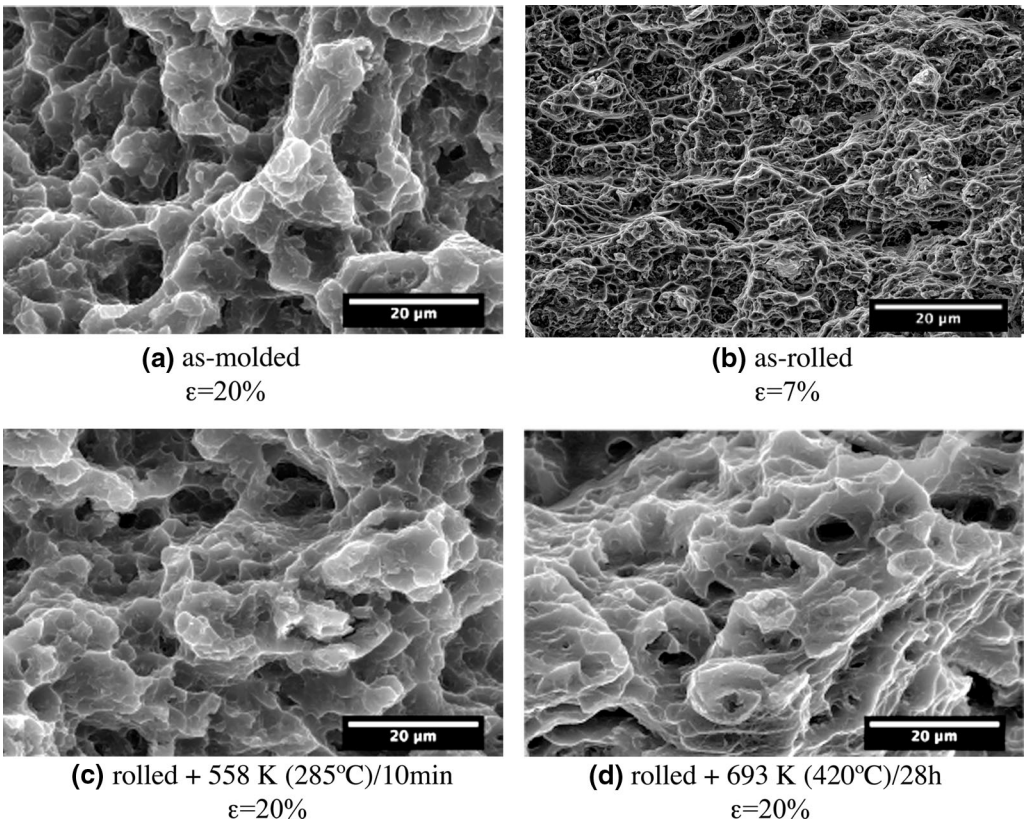

Fig. 11—SE images of fracture surfaces in (*a*) as-molded plate, (*b*) as-rolled sheet, and sheets annealed for (*c*) 558 K (285 °C) for 10 min and (*d*) 693 K (420 °C) for 28 h.

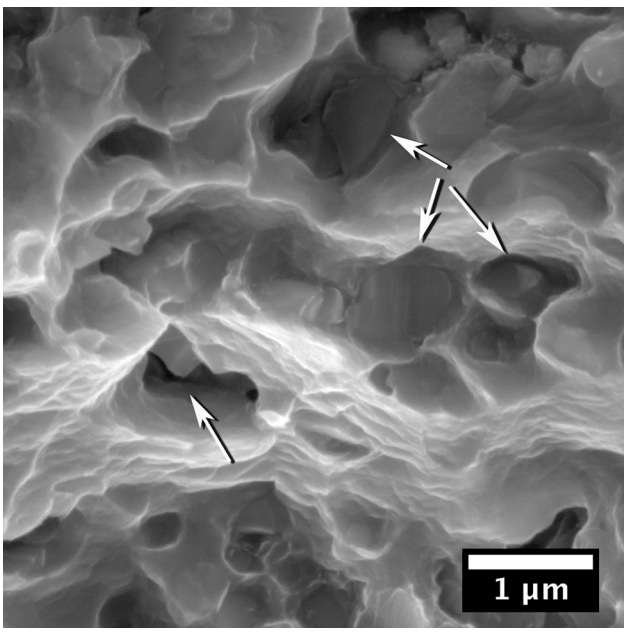

Fig. 12—SE micrograph of fragmented β-particles at the bottom of voids in the sheet annealed for 558 K (285 °C) for 10 min.

ed the yield strength as well. In conditions where fewer grains were oriented for easy, basal slip, the yield strength increases. Similarly, work hardening is also dependent on both grain size and texture. The low basal texture intensity is associated with *r* values favorable for formability. The balance of strength and ductility combined with the low *r* values in the annealed sheets indicates that TTMP can provide Mg sheet with better formability than conventional AZ31.

During tensile deformation, damage accumulates preferentially in the β-phase particles. However, this damage does not lead to premature failure and low ductility. The average ductility to failure was nominally 23 pct in the annealed sheets, regardless of grain size, β-phase volume fraction, or loading orientation. Failure results from coalescence of voids in the α-Mg matrix.

Processes such as TTMP, which allow for grain refinement without producing a strong basal texture, are essential to produce high strength Mg alloy sheet with isotropic formability. Inclusion of secondary phase particles, such as the β-$Mg_{17}Al_{12}$ particles studied in this work, has the potential to provide added microstructure control without sacrificing ductility.

ACKNOWLEDGMENTS

The authors express their gratitude to Raymond Decker and nanoMAG, LLC. for supplying the material and providing valuable feedback and discussions. In addition, we would like to recognize William Donlon for his contributions. This study was partially

funded by the National Science Foundation (Grant No. 0847198).

REFERENCES

1. J.A. Chapman and D.V. Wilson: *J. Inst. Met.*, 1962, vol. 91, pp. 39–40.
2. M.R. Barnett, D.L. Atwell, and A.G. Beer: *Mater. Sci. Forum*, 2007, vols. 558–559, pp. 433–40.
3. A. Yamashita, Z. Horita, and T. Langdon: *Mater. Sci. Eng. A*, 2001, vol. 300, pp. 142–47.
4. C.D. Lee: *Mater. Sci. Eng. A*, 2007, vol. 459, pp. 355–60.
5. A. Jain, O. Duygulu, D. Brown, C. Tomé, and S.R. Agnew: *Mater. Sci. Eng. A*, 2008, vol. 486, pp. 545–55.
6. B.Q. Shi, R.S. Chen, and W. Ke: *J. Magnes. Alloy.*, 2013, vol. 1, pp. 210–16.
7. A. Sadeghi, S. Shook, and M. Pekguleryuz: *Mater. Sci. Eng. A*, 2011, vol. 528, pp. 7529–36.
8. Q. Miao, L.X. Hu, G.J. Wang, and E. Wang: *Mater. Sci. Eng. A*, 2011, vol. 528, pp. 6694–01.
9. C.W. Chung, R.G. Ding, Y. Chino, M.A. Hodgson, and W. Gao: *IOP Conf. Ser. Mater. Sci. Eng.*, 2009, vol. 4, p. 012012.
10. T. Mukai, T. Mohri, M. Mabuchi, M. Nakamura, K. Ishikawa, and K. Higashi: *Scripta Mater.*, 1998, vol. 39, pp. 1249–53.
11. R. Gehrmann, M. Frommert, and G. Gottstein: *Mater. Sci. Eng. A*, 2005, vol. 395, pp. 338–49.
12. S.R. Agnew, J.A. Horton, T.M. Lillo, and D.W. Brown: *Scripta Mater.*, 2004, vol. 50, pp. 377–81.
13. T. Mukai, H. Watanabe, K. Ishikawa, and K. Higashi: *Mater. Sci. Forum*, 2003, vols. 419–422, pp. 171–76.
14. D. Wu, R.S. Chen, and E.H. Han: *J. Alloys Compd.*, 2011, vol. 509, pp. 2856–63.
15. N. Stanford and M.R. Barnett: *J. Alloys Compd.*, 2008, vol. 466, pp. 182–88.
16. N. Stanford, D. Atwell, and M.R. Barnett: *Acta Mater.*, 2010, vol. 58, pp. 6773–83.
17. F.J. Humphreys and M. Hatherly: *Recrystallization and Related Annealing Phenomena*, 2nd ed., Elsevier, Amsredam, 2004.
18. J.P. Hadorn, K. Hantzsche, S.B. Yi, J. Bohlen, D. Letzig, and S.R. Agnew: *Metall. Mater. Trans. A*, 2012, vol. 43A, pp. 1363–75.
19. A. Luo: *Metall. Mater. Trans. A*, 1995, vol. 26A, pp. 2445–55.
20. C.D. Lee: *Met. Mater. Int.*, 2010, vol. 16, pp. 543–51.
21. Y.Z. Lu, Q.D. Wang, W.J. Ding, X.Q. Zeng, and Y.P. Zhu: *Mater. Lett.*, 2000, vol. 44, pp. 265–68.
22. C.D. Lee and K.S. Shin: *Met. Mater. Int.*, 2003, vol. 9, pp. 21–27.
23. B. Chen, D.L. Lin, L. Jin, X.Q. Zeng, and C. Lu: *Mater. Sci. Eng. A*, 2008, vols. 483–484, pp. 113–16.
24. H.A. Patel, D.L. Chen, S.D. Bhole, and K. Sadayappan: *J. Alloys Compd.*, 2010, vol. 496, pp. 140–48.
25. Q. Guo, H.G. Yan, Z.H. Chen, and H. Zhang: *Trans. Nonferrous Met. Soc. China*, 2006, vol. 16, pp. 922–26.
26. J. Song, S.M. Xiong, M. Li, and J.E. Allison: *Mater. Sci. Eng. A*, 2009, vol. 520, pp. 197–201.
27. R.F. Decker, S. Kulkarni, and J. Huang: *Magnesium Technology 2009: Proc. TMS*, E.A. Nyberg, S.R. Agnew, N.R. Neelameggham, and M.O. Pekguleryuz, eds., TMS, Warrendale, PA, 2009, pp. 357–61.
28. J. Huang, T. Arbel, L. Ligeski, J. Mccaffrey, S. Kulkarni, J.W. Jones, T.M. Pollock, R.F. Decker, and S. Lebeau: *Magnesium Technology 2010: Proc. TMS*, S.R. Agnew, N.R. Neelameggham, E.A. Nyberg, and W.H. Sillekens, eds., TMS, Warrendale, PA, 2010, pp. 489–93.
29. R.F. Decker: *Solid State Phenom.*, 2012, vols. 192–193, pp. 47–57.
30. F. Czerwinski, A. Zielinska-Lipiec, P.J. Pinet, and J. Overbeeke: *Acta Mater.*, 2001, vol. 49, pp. 1225–35.
31. T.D. Berman, W. Donlon, R.F. Decker, J. Huang, T.M. Pollock, and J.W. Jones: *Magnesium Technology 2011: Proc. TMS*, W.H. Sillekens, S.R. Agnew, N.R. Neelameggham, and S.N. Mathaudhu, eds., Wiley, Hoboken, NJ, 2011, pp. 599–603.
32. T.D. Berman, W. Donlon, R.F. Decker, J. Huang, T.M. Pollock, and J.W. Jones: *Magnesium: Proc. 9th Int. Conf. Magnesium Alloys and Their Applications*, W.J. Poole and K.U. Kainer, eds., ICMAA2012, Vancouver, 2012, pp. 571–78.
33. T.D. Berman, W. Donlon, V.M. Miller, R.F. Decker, J. Huang, T.M. Pollock, and J.W. Jones: *Magnesium Technology 2012: Proc. TMS*, S.N. Mathaudhu, W.H. Sillekens, N. Hort, and N.R. Neelameggham, eds., Wiley, Hoboken, 2012, pp. 339–44.
34. T.D. Berman, W. Donlon, C.K. Hung, P. Milligan, R.F. Decker, T.M. Pollock, and J.W. Jones: *Magnesium Technology 2013: Proc. TMS*, N. Hort, S.N. Mathaudhu, N.R. Neelameggham, and M. Alderman, eds., Wiley, Hoboken, 2013, pp. 113–18.
35. T.D. Berman, W. Donlon, R.F. Decker, T.M. Pollock, and J.W. Jones: *Magnesium Technology 2014: Proc. TMS*, M. Alderman, M.V. Manuel, N. Hort, and N.R. Neelameggham, eds., Wiley, Hoboken, 2014, pp. 161–66.
36. A.A. Nayeb-Hashemi: *Phase Diagrams of Binary Magnesium Alloys*, ASM International, Metals Park, 1988.
37. W.T. Lankford, S.C. Snyder, and J.A. Bauscher: *Trans. Am. Soc. Met.*, 1950, vol. 42, pp. 1197–32.
38. T.D. Berman: Ph.D. Thesis, University of Michigan, Ann Arbor, 2014.
39. F. Bachmann, R. Hielscher, and H. Schaeben: *Solid State Phenom.*, 2010, vol. 160, pp. 63–68.
40. G. Proust, C.N. Tomé, and G.C. Kaschner: *Acta Mater.*, 2007, vol. 55, pp. 2137–48.
41. B.S. Fromm, B.L. Adams, S. Ahmadi, and M. Knezevic: *Acta Mater.*, 2009, vol. 57, pp. 2339–48.
42. W. Yuan, S.K. Panigrahi, J.-Q. Su, and R.S. Mishra: *Scripta Mater.*, 2011, vol. 65, pp. 994–97.
43. G. Bhargava, W. Yuan, S.S. Webb, and R.S. Mishra: *Metall. Mater. Trans. A*, 2009, vol. 41A, pp. 13–17.
44. N. Stanford and M.R. Barnett: *Int. J. Plast*, 2013, vol. 47, pp. 165–81.
45. M.R. Barnett, Z. Keshavarz, A.G. Beer, and D. Atwell: *Acta Mater.*, 2004, vol. 52, pp. 5093–03.
46. J. Bohlen, P. Dobron, J. Swiostek, D. Letzig, F. Chmelik, P. Lukac, and K.U. Kainer: *Mater. Sci. Eng. A*, 2007, vol. 462, pp. 302–06.
47. L.L. Chang, Y.N. Wang, X. Zhao, and M. Qi: *Mater. Charact.*, 2009, vol. 60, pp. 991–94.
48. Y. Chino, M. Mabuchi, R. Kishihara, H. Hosokawa, Y. Yamada, C. Wen, K. Shimojima, and H. Iwasaki: *Mater. Trans.*, 2002, vol. 43, pp. 2554–60.
49. J.A. del Valle, F. Carreño, and O.A. Ruano: *Acta Mater.*, 2006, vol. 54, pp. 4247–59.
50. W.J. Kim, J.B. Lee, W.Y. Kim, H.T. Jeong, and H.G. Jeong: *Scripta Mater.*, 2007, vol. 56, pp. 309–12.
51. N. Ono, K. Nakamura, and S. Miura: *Mater. Sci. Forum*, 2003, vols. 419–422, pp. 195–200.
52. W.J. Kim, C.W. An, Y.S. Kim, and S.I. Hong: *Scripta Mater.*, 2002, vol. 47, pp. 39–44.
53. C.D. Lee: *Mater. Sci. Eng. A*, 2007, vols. 454–455, pp. 575–80.
54. P. Sharifi, Y. Fan, J.P. Weiler, and J.T. Wood: *J. Alloys Compd.*, 2014, vol. 605, pp. 237–43.
55. Y. Chino and M. Mabuchi: *Adv. Eng. Mater.*, 2001, vol. 3, pp. 981–83.
56. R.W. Armstrong: *Acta Metall.*, 1968, vol. 16, pp. 347–55.
57. G. Sambasiva Rao and Y.V.R.K. Prasad: *Metall. Trans. A*, 1982, vol. 13A, pp. 2219–26.
58. S.R. Agnew: *Magnesium Technology 2002: Proc. TMS*, H.I. Kaplan, ed., TMS, Warrendale, PA, 2002, pp. 169–74.
59. J. Bohlen, M.R. Nurnberg, J.W. Senn, D. Letzig, and S.R. Agnew: *Acta Mater.*, 2007, vol. 55, pp. 2101–12.
60. S.R. Agnew and O. Duygulu: *Int. J. Plast*, 2005, vol. 21, pp. 1161–93.
61. Y. Chino, H. Iwasaki, and M. Mabuchi: *Mat. Sci. Eng. A*, 2007, vol. 466, pp. 90–95.
62. S.B. Yi, J. Bohlen, F. Heinemann, and D. Letzig: *Acta Mater.*, 2010, vol. 58, pp. 592–605.
63. Y. Liu and X. Wu: *Metall. Mater. Trans. A*, 2006, vol. 37A, pp. 7–17.
64. J. Koike and R. Ohyama: *Acta Mater.*, 2005, vol. 53, pp. 1963–72.
65. T. Ebeling, Ch. Hartig, and R. Bormann: *Magnesium Technology 2010: Proc. TMS*, S.R. Agnew, N.R. Neeglameggham, E.A. Nyberg, and W. Sillekens, eds., Hoboken, 2010, pp. 521–25.
66. J. Koike, Y. Sato, and D. Ando: *Mater. Trans.*, 2008, vol. 49, pp. 2792–2800.
67. J. Koike: *Acta Mater.*, 2003, vol. 51, pp. 2055–65.

68. M.A. Meyers, O. Vöhringer, and V.A. Lubarda: *Acta Mater.*, 2001, vol. 49, pp. 4025–39.
69. D.B. Lewis and F.B. Pickering: *Met. Technol.*, 1983, vol. 10, pp. 264–73.
70. H. Inoue and T. Takasugi: *Mater. Trans.*, 2007, vol. 48, pp. 2014–22.
71. W.F. Hosford: *The Mechanics of Crystals and Textured Polycrystals*, Oxford University Press, New York, 1993.
72. X.S. Huang, K. Suzuki, Y. Chino, and M. Mabuchi: *J. Alloys Compd.*, 2011, vol. 509, pp. 7579–84.
73. X.S. Huang, K. Suzuki, and N. Saito: *Scripta Mater.*, 2009, vol. 60, pp. 651–54.
74. Y. Chino, K. Sassa, and M. Mabuchi: *J. Mater. Sci.*, 2009, vol. 44, pp. 1821–27.
75. H. Zhang, G.S. Huang, D.Q. Kong, G.F. Sang, and B. Song: *J. Mater. Process. Technol.*, 2011, vol. 211, pp. 1575–80.
76. Y. Chino and M. Mabuchi: *Scripta Mater.*, 2009, vol. 60, pp. 447–50.
77. X.S. Huang, K. Suzuki, A. Watazu, I. Shigematsu, and N. Saito: *J. Alloys Compd.*, 2009, vol. 470, pp. 263–68.
78. W.F. Hosford and R.M. Caddel: *Metal Forming: Mechanics and Metallurgy*, 2nd ed., Prentice Hall, Upper Saddle River, 1993, pp. 298–301.
79. S. Gall, R.S. Coelho, S. Müller, and W. Reimers: *Mater. Sci. Eng. A*, 2013, vol. 579, pp. 180–87.
80. T. Wu, L. Jin, W.X. Wu, L. Gao, J. Wang, Z.Y. Zhang, and J. Dong: *Mater. Sci. Eng. A*, 2013, vol. 584, pp. 97–102.
81. F. Kaiser, D. Letzig, J. Bohlen, A. Styczynski, Ch. Hartig, and K.U. Kainer: *Mater. Sci. Forum*, 2003, vols. 419–422, pp. 315–20.
82. W.F. Hosford: *Mater. Sci. Eng. A*, 1998, vol. 257, pp. 1–8.
83. M.R. Barnett: *Mater. Sci. Eng. A*, 2007, vol. 464, pp. 8–16.
84. M. Marya, L.G. Hector, R. Verma, and W. Tong: *Mater. Sci. Eng. A*, 2006, vol. 418, pp. 341–56.
85. Z. Chen, J. Huang, R.F. Decker, S.E. Lebeau, L.R. Walker, O.B. Cavin, T.R. Watkins, and C.J. Boehlert: *Metall. Mater. Trans. A*, 2010, vol. 42A, pp. 1386–1399.
86. Z.F. Li, J. Dong, X.Q. Zeng, C. Lu, and W.J. Ding: *Mater. Sci. Eng. A*, 2007, vol. 466, pp. 134–39.
87. A.N. Chamos, S.G. Pantelakis, G.N. Haidemenopoulos, and E. Kamoutsi: *Fatigue Fract. Eng. Mater. Struct.*, 2008, vol. 31, pp. 812–21.